Geophys. J. Int. (2002) **151,** 132–145

The *P* wavespeed structure below and around the Kaapvaal craton to depths of 800 km, from traveltimes and waveforms of local and regional earthquakes and mining-induced tremors

R. E. Simon,[1,2] C. Wright,[1] E. M. Kgaswane[1,*] and M. T. O. Kwadiba[1,3]

[1] *Bernard Price Institute of Geophysical Research, The University of the Witwatersrand, Johannesburg, Private Bag* 3, *Wits* 2050, *South Africa. E-mail: 006cwrig@cosmos.wits.ac.za*
[2] *Department of Physics, University of Botswana, Private Bag* 48707, *Gaborone, Botswana*
[3] *Department of Geological Survey, Private Bag* 14, *Lobatse, Botswana*

Accepted 2002 April 10. Received 2002 March 20; in original form 2001 July 18

SUMMARY

An average *P*-wavespeed model from the surface to depths of 800 km was derived for southern Africa using traveltimes and waveforms from earthquakes recorded at stations of the Kaapvaal and South African National networks. In this first study of the transition zone for the central part of the African superswell, a damped least-squares inversion was used to minimize effects of origin time errors. Triplications were observed for both the 410 and 670 km discontinuities, with crossover points between first arrival branches at average distances of 19.61° and 23.92°, respectively. The Herglotz–Wiechert method combined with ray tracing was used to derive a preliminary model, followed by refinements using phase-weighted stacking and synthetic seismograms to yield the final model BPI1A. This model shows a prominent 410 km discontinuity, but a weakly-defined 670 km discontinuity, in agreement with the SATZ model for a region of southern Africa to the north of the region covered by the present study. The wavespeeds of BPI1A from the base of the crust to 270 km depth lie between those of the SATZ model and the IASP91 model, which have higher and lower wavespeeds respectively. Between depths of 270 km and the 410 km discontinuity, models BPI1A, IASP91 and SATZ have similar wavespeeds but the 410 km discontinuity for BPI1A is about 10 km deeper than in IASP91. Model GNEM for Eurasia has lower wavespeeds than the other three models above the 410 km discontinuity. Within the transition zone models BPI1A and SATZ converge as the depth increases, with wavespeeds that exceed those of IASP91 below 500 km depth. These models and model GNEM all have similar wavespeeds below 750 km depth. The seismic results indicate no regions of anomalous low wavespeeds within the uppermost 800 km of the mantle that could be associated with high temperatures and the uplift of the African superswell. However, higher seismic wavespeeds in the transition zone than elsewhere are suggested for the southern part of the region, which may result from iron depletion and therefore lower densities that might contribute to buoyant uplift of the overlying crust and upper mantle.

Key words: Kaapvaal craton, seismic wavespeeds, transition zone, upper mantle.

INTRODUCTION

The region of study shown in Fig. 1 is dominated by the Kaapvaal craton, which formed and stabilized between 3.7 and 2.7 Ga, and is one of the oldest reasonably sized examples of an Archaean craton (de Wit *et al.* 1992). To the north, the craton is bounded by the Limpopo belt, which separates it from the Zimbabwe craton; to the west and south, it is bordered by Proterozoic mobile belts, and to the east by the Lebombo monocline of Jurassic volcanics associated with the break-up of Gondwana (de Wit *et al.* 1992). The mantle beneath southern Africa has not been extensively studied using broad-band data compared with other continental regions. Cattermole (1994) used data from five stations from a broad-band network of eight stations to investigate mantle structure beneath South Africa, by analysing seismic waves converted from *P* to *SV* at discontinuities. His results revealed a complicated phase for the 410 km discontinuity and no phase for the 670 km discontinuity.

Vinnik *et al.* (1996) using the same stations as Cattermole found that the arrival time of the phase resulting from the *P* to *SV*

*Now at: Council for Geoscience, Private Bag X112, Pretoria 0001, South Africa

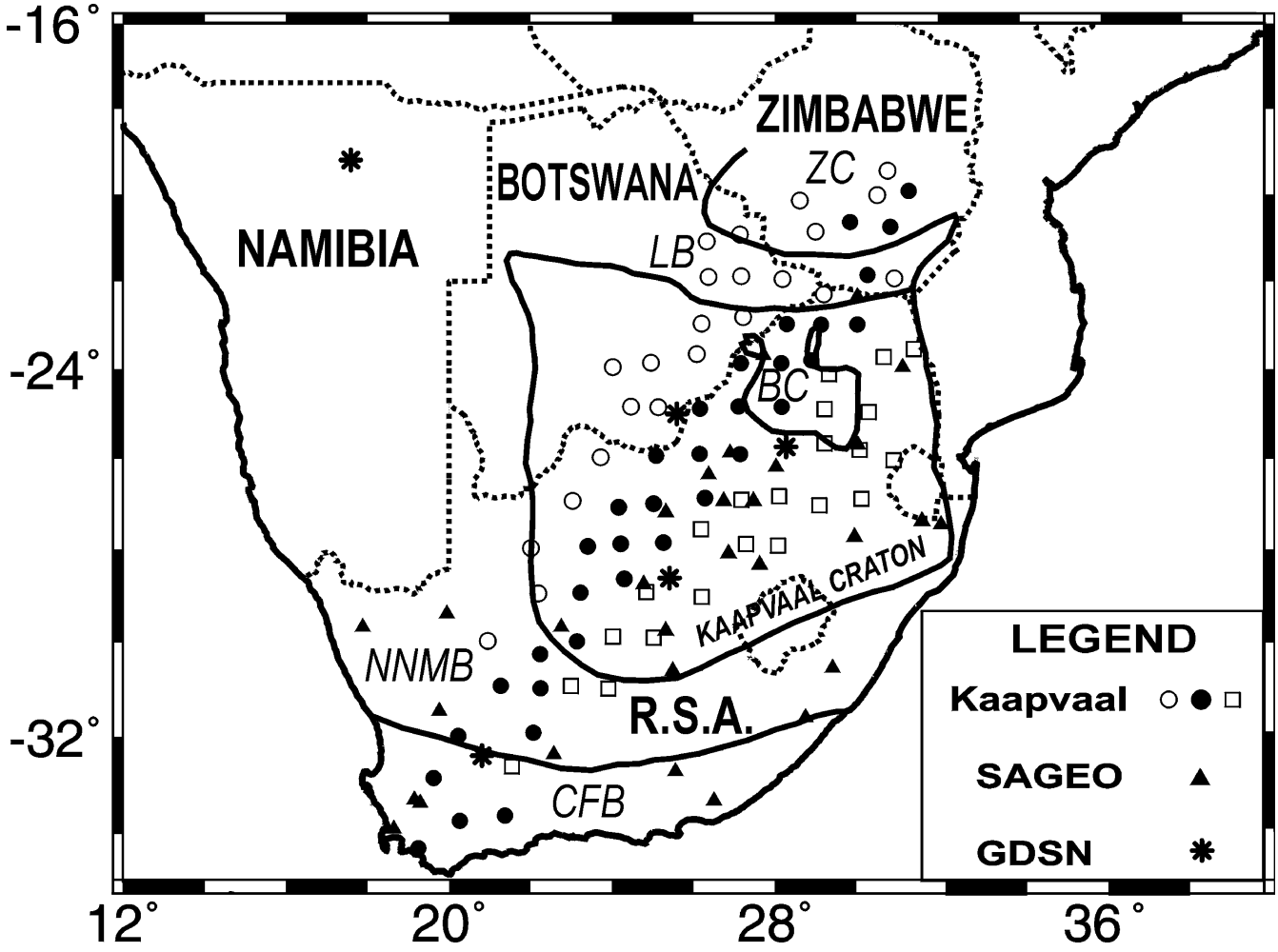

Figure 1. Map showing distribution of stations of the Kaapvaal craton network, permanent broadband stations and the South African National network, with main tectonic boundaries superimposed. CFB—Cape fold belt; NNMB—Namaqua-Natal mobile belt; LB—Limpopo belt; ZC—Zimbabwe craton. The lines surrounding BC define the approximate boundary for surface outcrops of the Bushveld complex. The map shows locations of stations with open circles, closed circles and open squares denoting stations deployed from April 1997-April 1998, April 1997-April 1999 and April 1998-April 1999, respectively. SAGEO—South African network; GDSN—Global Digital Seismological network.

conversion at the 670 km discontinuity is 2 s earlier than that predicted by earth model IASP91 (International Association of Seismology and Physics of the Earth's Interior 1991) of Kennett (1991). Vinnik *et al.* (1996) used observations of the teleseismic *P* to *SV* converted phases at a boundary 650 km depth, and proposed a model that provides a very good fit between the observed and synthetic waveforms of a phase with a downward motion at 38 s. Such motion is possible if the conversion occurs at the upper boundary of a low wavespeed layer. This structure is unusual, and needs confirmation using a larger broad-band network (Wright *et al.* 1997). Results from older broad-band data show some differences in mantle structure from those for other cratons (Green *et al.* 1995).

Wright *et al.* (2002) derived a *P* wavespeed model of the crust and upper mantle to depths of 320 km for southern Africa, but their interpretation emphasized the top 150 km: comparison of estimated crustal thicknesses with those from receiver functions, discussion of evidence for a low wavespeed layer in the mantle at depths between 65 and 120 km, and comparison of the average *P* wavespeed estimates with those estimated from mantle xenoliths. They also discussed the statistical approach to correcting for relative origin time errors between events recorded by the South African network, and the damped least-squares inversion procedure used to minimize origin time errors for events recorded by the Kaapvaal network.

In the present study, we take advantage of the high density of seismic stations and the high quality and great quantity of the database of seismograms from the Kaapvaal craton experiment to define an average *P* wavespeed structure below the Kaapvaal craton to depths of about 800 km. Compared with the previous studies for this area, the station coverage is considerably improved, not only in terms of separation between stations, but also in covering a wide area from Cape Town in South Africa to Masvingo in Zimbabwe (Fig. 1). Thus, data quantity and resolving power are greatly increased. Most papers discussing the deeper parts of the upper mantle and transition zone (for example, those published using events north of Australia e.g. Dey *et al.* 1993; Kennett *et al.* 1994) have to use an assumed model for the crust and shallow parts of the mantle. The difference of our work from most other studies of continental structure is that recorded seismic events provide continuous coverage from distances of 0 to 34 degrees, so that a complete *P* wavespeed structure can be derived for the region. Much of the published work for the southern African region is based on surface waves and there is very little on body waves which covers the transition zone. The only other work

of which we are aware, is the recent work by Zhao *et al.* (1999) that was based on data from the Tanzania craton broad-band seismic experiment conducted between 1994 and 1995 for examining lithospheric structure beneath the East African Plateau (Nyblade *et al.* 1996). Their region of study is farther north of the Zimbabwe craton shown in Fig. 1 and closer to the northern margin of the African superswell. Our work is concentrated on the central part of the superswell, for which it is important to map the transition zone to constrain uplift mechanisms for this region.

This work complements the previous studies by improving resolution of deep-seated subtle features. We compare the results with the preferred model (SATZ) of Zhao *et al.* (1999), because it was derived using a similar kind of data for a nearby region. The work by Zhao *et al.* (1999) is based on a relatively small data set, and exhibits a rather peculiar wavespeed structure around the 410 km discontinuity that looks quite different from those for other continental regions. We find that a critical step in using traveltimes to constrain mantle structure is to correct properly for errors in origin times between different seismic events, and this requires a damped least-squares inversion described in the paper by Wright *et al.* (2002). This situation arises because errors in origin times appear to be very serious in published epicentral data for the southern African region. No similar corrections were made by Zhao *et al.* (1999). A comparison of our work with the IASP91 model of Kennett (1991) is also provided, since it is a fairly recent reference wavespeed model in which the upper mantle component is weighted by data from both oceanic and continental regions. Finally, the recent GNEM model (Generalised Northern Eurasia Model) of Ryberg *et al.* (1998) for northern Eurasia allows a comparison with the upper mantle and transition zone below a cratonic region in a different part of the world.

DATA ACQUISITION AND SELECTION

Data used in this study are from local and regional earthquakes and mining-induced tremors recorded by the Kaapvaal craton broad-band seismic network supplemented by data from the South African National network at distances less than 10°. The Kaapvaal network consisted of approximately eighty broad-band stations that formed part of the international Kaapvaal craton programme (Carlson *et al.* 1996). The seismometers were deployed at locations across southern Africa from April 1997 through April 1999, with about fifty stations operating at any one time (Fig. 1).

The three-component digital data were recorded continuously at 20 samples per second. The broad-band seismometers formed a grid network with an average spacing of about 100 km. The sensors were coupled to the bedrock by creating a vault at a depth of around 70 cm and thermally insulating it from the surface environment. Of the eighty sites that were occupied during the two-year period of the project, 33 instruments were operational for the whole two years. An additional 23 instruments that were installed during the first year of deployment were later moved to cover new sites during the second year of deployment (Fig. 1). The majority of the local seismic sources used to constrain shallow structure is mining-induced, whereas the regional and teleseismic events are tectonic earthquakes.

We selected broad-band seismograms of earthquakes at maximum epicentral distances of 34° from the Kaapvaal stations. This experiment recorded many tectonic earthquakes occurring on the African continent and below the surrounding oceans. 15 of the largest of these were used in this study (Table 1 and Fig. 2). Mining-induced tremors that occurred on the periphery of the Witwatersrand basin (Table 1) and both mining-induced and tectonic events recorded by the South African network form the rest of the data used in this study. The tectonic events are shown as stars in Fig. 2, and the four regions of mining-induced events (East and Central Rand, West and Far West Rand, Klerksdorp and Welkom) are represented by the enclosed area containing four asterisks. The closed and open circles denote the mid-points of source–receiver paths for first arrival energy from the tectonic events that have penetrated to upper mantle depths, and to transition zone and lower mantle depths respectively.

METHODS OF DATA ANALYSIS

The data were analysed by interactive picking of the arrival times, on displays of record sections from stations of the Kaapvaal seismic network. Hypocentral data were obtained from the Preliminary Determination of Epicenter bulletins issued by the United States Geological Survey. For events beyond 15° distance, stacking was used to identify later arrival branches associated with the 410 and 670 km discontinuities. Since the events used are shallow and with complicated source functions, noise, particularly signal-generated noise, masks the later arrivals of interest. The signals were therefore bandpass filtered from 0.4 and 4.0 Hz before picking the first arrivals, which suppresses much of the noise field. For arrivals at distances less than 15°, no later arrivals other than *PmP* and *Pg* at short distances (<5°) were identified.

We use information in the waveforms on later arrivals associated with triplications that sample mainly the lowermost upper mantle, transition zone and uppermost lower mantle. To optimize use of this information, we processed the first 30 s of the *P*-wave train for selected events. A reference trace of less than two seconds length was selected for the first arrival of each event, and all other traces were cross-correlated against it, to determine the time shift to apply to each trace to give the best possible alignment (McQuillin *et al.* 1984). This removes differences in times between stations due to variations in underlying structure. For cross-correlation purposes, the traces used were restricted to distance ranges of less than two degrees to minimize differences in waveforms caused by scattering and attenuation, and time shifts were applied to correspond to a specified slowness defined by the measured traveltimes.

After cross-correlation, the seismograms were stacked at different slownesses relative to the first arrival at intervals of 0.1 s deg^{-1} from -1.5 to 1.5 s deg^{-1} to enhance coherent signals at the expense of noise. Resolution of later coherent arrivals has been improved by using the phase-weighted stacking technique (Schimmel & Paulssen 1997) to identify later body-wave arrivals of different slownesses associated with the upper-mantle triplications for both the 410 and 670 km discontinuities. The phase-weighted stack (PWS) employs the phase stack as a time-dependent weight of the linear stack. Every sample of the linear stack is weighted by the coherence of its instantaneous phase. The phase stack acts as a filter with a certain sharpness of the transition between phase similarity and dissimilarity, controlled by a certain power, ν (Schimmel & Paulssen 1997). The optimum choice of power used for the PWS was $\nu = 2$ which can be regarded as the power of the phase stack that satisfactorily increases the signal-to-noise ratio without causing too much signal distortion. For comparison the linear stack was retrieved with $\nu = 0$. Because of the problem of coherence of the first arrivals when stacking data over large distance ranges, phase-weighted stacks were also performed over ranges of less than two degrees. Stacking produces clearly identifiable later phases that are not visible on the original seismograms. We then searched for a pattern of later arrivals that is

Table 1. List of events recorded by the Kaapvaal craton network and used in traveltime and waveform analyses.

Event name	Event location	Date (d/m/y)	Origin time	Mag (local or body wave)	Depth (km)	Lat. S	Long. E	Dist. range (deg)
97112	Central Rand*	22/04/97	20 h 12 m 13.0 s	2.6	2	26.13	27.72	0.56–7.10
97143	Far West Rand*	23/05/97	10 h 58 m 57.6 s	2.8	2	26.43	27.47	0.54–7.20
97123	East Rand*	03/05/97	08 h 46 m 05.0 s	2.8	2	26.20	28.18	0.97–7.41
97127	Far West Rand*	07/05/97	10 h 04 m 28.4 s	3.9	2	26.38	27.51	0.58–7.52
97185	Klerksdorp*	04/07/97	00 h 48 m 10.1 s	3.7	2	26.74	26.82	0.49–8.10
97233	Klerksdorp*	21/08/97	15 h 00 m 31.6 s	3.2	2	26.92	26.80	0.46–8.27
97137	Far West Rand*	17/05/97	10 h 32 m 30.8 s	3.2	2	26.39	27.44	0.64–8.39
97133	Far West Rand*	13/05/97	01 h 01 m 55.9 s	3.3	2	26.37	27.42	0.63–8.41
97207	West Rand*	26/07/97	03 h 22 m 42.2 s	3.5	2	26.42	27.66	0.65–8.54
97161	West Rand*	10/06/97	23 h 27 m 24.3 s	3.4	2	26.41	27.66	0.68–8.54
97162	Klerksdorp*	11/06/97	13 h 06 m 51.7 s	2.9	2	26.25	27.67	0.58–8.66
97237	East Rand*	25/08/97	18 h 41 m 16.4 s	3.8	2	26.18	28.22	1.00–9.07
97168	Welkom*	17/06/97	18 h 11 m 13.6 s	3.1	2	27.99	26.68	1.17–9.27
97125	Welkom*	05/05/97	21 h 28 m 33.5 s	3.1	2	27.99	26.63	1.16–9.29
98003	Malawi	03/01/98	03 h 05 m 52.3 s	4.6	33	15.80	35.02	5.43–20.99
98236	Malawi	24/08/98	12 h 12 m 09.5 s	4.8	46	13.79	34.73	6.80–24.84
97283	Democratic Rep. of the Congo	10/10/97	06 h 25 m 55.9 s	4.8	33	11.79	28.70	7.89–20.94
98287	West of Cape Town	14/10/98	22 h 48 m 06.5 s	4.8	10	34.62	8.89	8.56–24.57
97264	Lake Tanganyika	21/09/97	18 h 13 m 22.7 s	5.7	10	7.36	30.37	12.04–25.62
98087	Lake Tanganyika	28/03/98	21 h 59 m 56.1 s	5.3	10	6.02	29.53	13.42–27.45
98116	Congo Region	26/04/98	14 h 16 m 52.2 s	5.5	10	−0.86#	17.34	19.29–32.89
97118	Prince Edward Is.	28/04/97	12 h 07 m 36.0 s	5.7	10	42.50	42.69	19.77–25.26
97180	Botswana-Zimbabwe Border+	29/06/97	17 h 32 m 07.0 s	4.0	5	20.34	27.22	0.59–13.29
98265	Madagascar	22/09/98	19 h 27 m 30.4 s	4.7	10	20.15	45.35	13.74–27.05
98014	Prince Edward Is.	14/01/98	02 h 37 m 03.8 s	5.8	10	39.61	46.36	21.01–25.19
98200	South of Africa	19/07/98	18 h 13 m 42.1 s	4.9	10	48.14	31.67	16.41–28.04
97253a	South of Africa	10/09/97	22 h 29 m 26.7 s	5.3	10	52.91	19.72	21.05–34.46
97253b	South of Africa	10/09/97	20 h 27 m 41.0 s	5.1	10	52.80	19.68	20.95–34.37
98064	Congo Region	05/03/98	02 h 59 m 43.3 s	5.4	10	−0.81#	17.42	23.45–32.84

*Location from Council for Geoscience Bulletins.
+Location using data from Kaapvaal network; locations of all other events from United States Geological Survey Bulletins.
#Latitude north.

consistent with predicted arrival times from ray theory and relative amplitudes estimated from synthetic seismograms.

For each event, relative origin time corrections for events recorded by the Kaapvaal network were estimated using a modification of part of the LSDARC method of shallow seismic refraction analysis (Wright 1999) using as input data only times at distances greater than 1.80°, corresponding to ray paths through the mantle. A detailed description of the basic idea of the method used to estimate the baseline corrections for each event has been provided in Wright *et al.* (2002). The measured times from tectonic events used were all corrected for focal depth by ray tracing to correspond to surface-to-surface times. However, the method of estimating relative baseline corrections compensates for this effect, so that the traveltime curve obtained when no focal depth corrections were applied was virtually indistinguishable from the curve of Fig. 3. Furthermore, at distances less than 10° the traveltimes were supplemented by times measured at short-period seismic stations of the South African National network (Wright *et al.* 2002). All the corrected first-arrival times used in the traveltime analysis from both the South African and Kaapvaal networks are shown in Fig. 3 and overlain with the reduced traveltime curve from model BPI1A ($V_{red} = 10.0$ km s^{-1}). Because the data used in this study differ slightly from those of Wright *et al.* (2002), due to the addition of two extra events at distances less than 20° (events 98200 and 98265 in Table 1), so that the wavespeeds in the crust and upper-mantle also show small differences from BPI1, we denote the present model BPI1A.

We first consider the fitting of a smooth curve through the corrected traveltimes at distances less than the crossover point for the triplication produced by the 410 km discontinuity which occurs at offset of about 19.61°. A fourteenth degree polynomial was fitted through the data and is shown as a reduced traveltime curve in Fig. 4. Note the hump in the reduced traveltime curve at distances between 1.62° and 2.88°, explained as being due to the low amplitude of the *Pn* arrival in this distance range, resulting in the frequent picking of later arrival energy as the first arrival phase. To extend the fitting of a smooth curve through the corrected traveltimes beyond distances of 19.61°, a sixth-degree polynomial was fitted through the data and is shown as a reduced traveltime curve in Fig. 5. The fitting of different polynomials was necessary because fitting a single high-degree polynomial over the entire distance range resulted in spurious oscillations in the curve at higher distances where the data were sparse and unevenly distributed.

To test the robustness of the polynomial fit, we have used a completely different mathematical approach to fit the smooth curves at distances greater than 1.08°. The method of summary values (Jeffreys 1937, 1961; Bolt 1978) was used, and differs from polynomial fitting in that there is a certain amount of flexibility in the details of the curve fitting. The results are shown in Fig. 6, in which

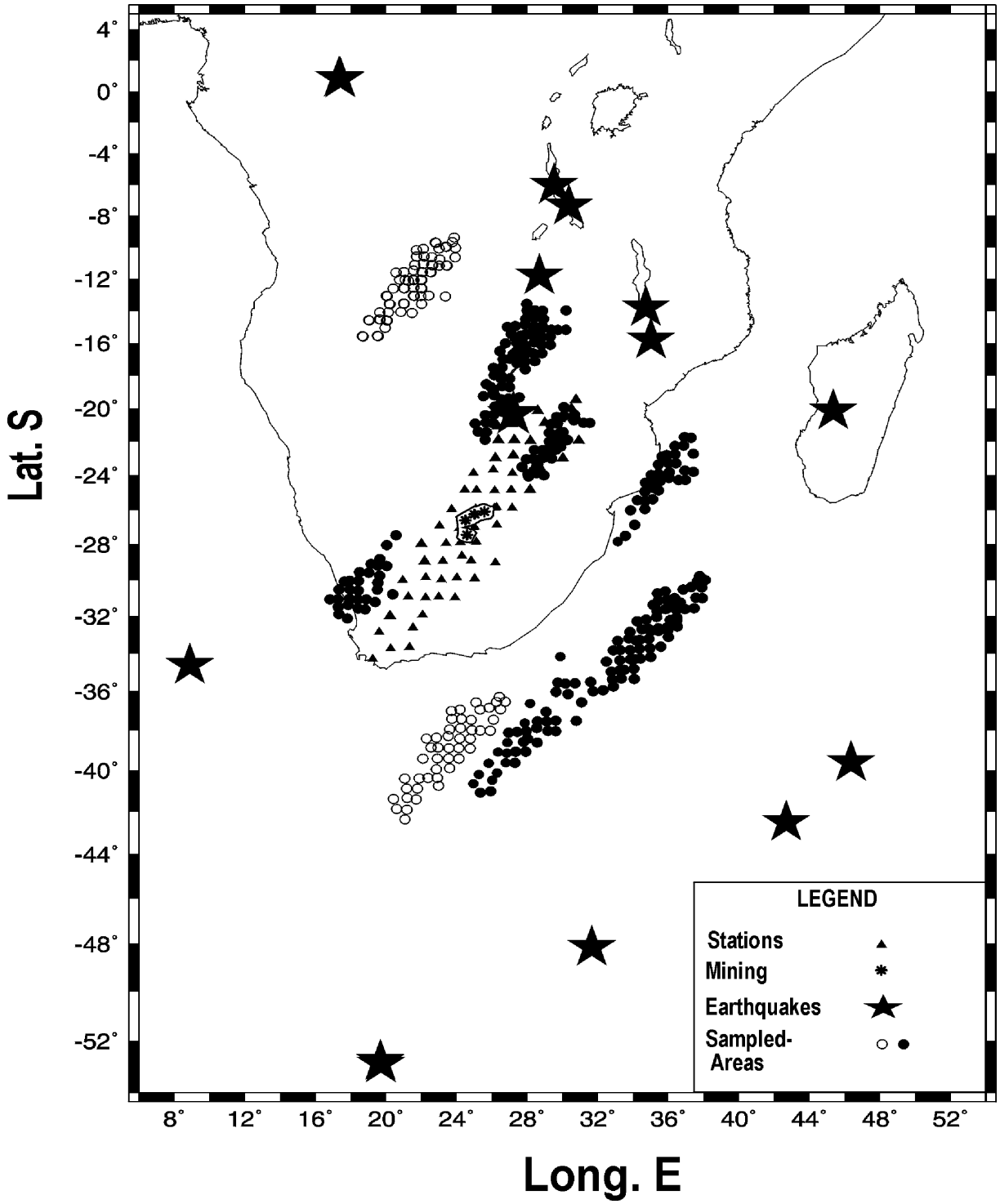

Figure 2. Map showing locations of mine tremors and earthquakes used in the present study. The four enclosed small stars show the main areas of mining-induced seismicity: from bottom to top—Welkom, Klerksdorp, Far West and West Rand, Central and East Rand. The map shows big stars, triangles, closed circles and open circles denoting earthquake sources, Kaapvaal station locations, sampled areas above and within the transition zone and sampled areas below the transition zone, respectively. The circles define the mid-points between sources and stations.

the summary points with standard errors are plotted together with a weighted cubic spline fitted through the points with just a small amount of smoothing using the algorithm of Reinsch (1967). The results show near perfect agreement with the polynomial fit, except at distances less than 2.70°, where the data were deliberately over-smoothed to suppress the amplitude of the hump (Fig. 4).

An important step in the construction of the average model, BPI1A, is to evaluate the Herglotz–Wiechert integral (Aki & Richards 1980, pp. 643–651) over the distance range greater than 19.61°. The shallow wavespeed structure is a modified version of the earlier work of Wright *et al.* (2002) that takes into account the improved resolution obtained by adding new data at shorter distances.

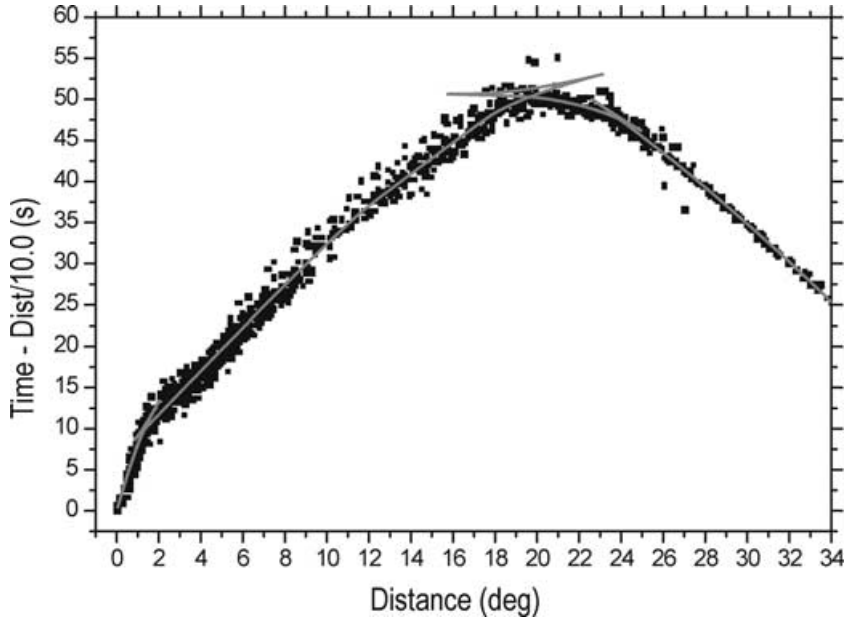

Figure 3. Plot showing all first-arrival times used in the travel-time analysis from both the South African and Kaapvaal networks, with baseline corrections, and overlain with the reduced traveltime curve from model BPI1A ($V_{red} = 10.0$ km s^{-1}). 'Dist' in reduced times refers to distance in kilometres.

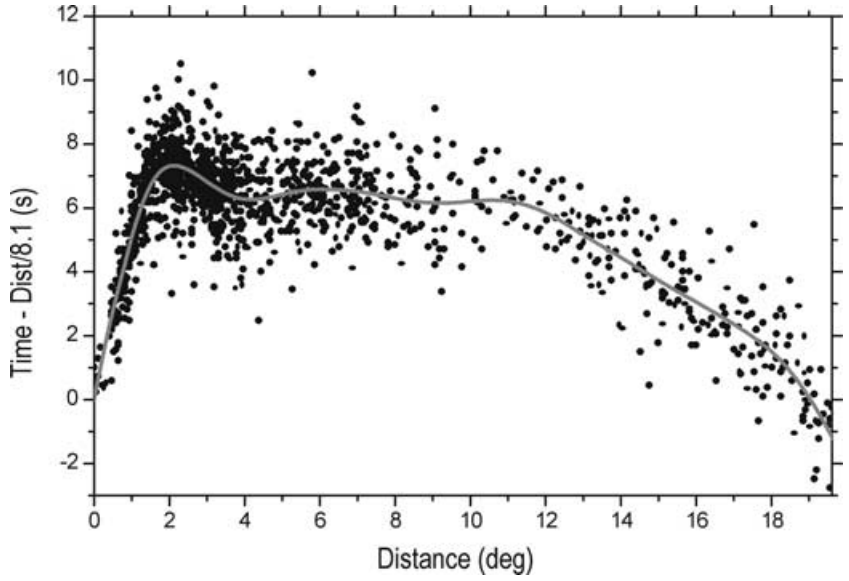

Figure 4. Combined time data from the Kaapvaal and South African networks in the distance range 0–19.61°. The smooth curve is a polynomial of degree 14 fitted over the same distance range, but plotted between 1.08° and 19.61°. At distances between 0° and 1.08°, a second degree polynomial was fitted through the data so that it has the same slope and time value at the join, and has a slope at 0 km that corresponds to a surface wavespeed of 5.58 km s^{-1}.

The deeper part of the model was then constructed by evaluating the Herglotz–Wiechert integral on an earth 'stripped' to 120 km depth to provide a preliminary smooth model using the slowness curves constructed from the spline fits to the data between 12° and 20°, and between 20° and 34°. This preliminary model was followed by refinements using later arrival times obtained from the phase-weighted stack and synthetic seismograms, to introduce the triplications associated with the major discontinuities. The synthetic seismograms were generated using the WKBJ technique (Chapman 1978), and show, in an appropriate manner, the relative amplitudes of the branches associated with the triplications. Traveltime calculations based on ray theory tell us very little about amplitudes. However, the synthetic seismograms enable us to determine in a more reliable manner the distance ranges over which later arrivals might be observable for a particular wavespeed model. They therefore assist in interpreting the results from phase-weighted stacking. The resulting wavespeed distribution was perturbed to fit curves of both the reduced traveltimes and slownesses generated from the summary values method (Figs 6 and 7). The gradient of a particular discontinuity was adjusted to match the later arrival times from the PWS and synthetic seismograms as closely as possible. This was achieved by taking the preliminary model, imposing either an abrupt or transitional wavespeed change at the discontinuity, and varying the wavespeeds above and below the discontinuity. Then

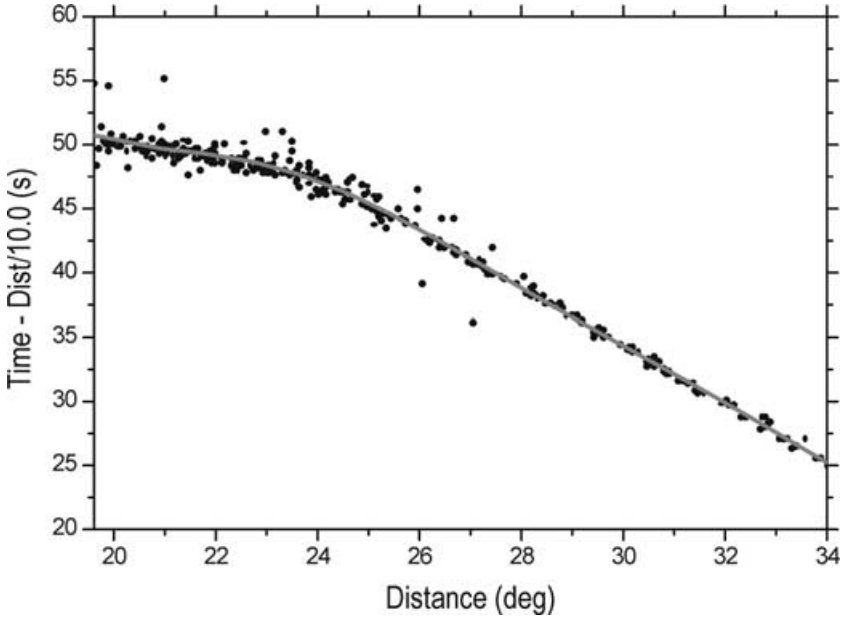

Figure 5. First arrival time data from the Kaapvaal network in the distance range 19.61°–34°. The smooth curve is a polynomial of degree 6 fitted over the same distance range.

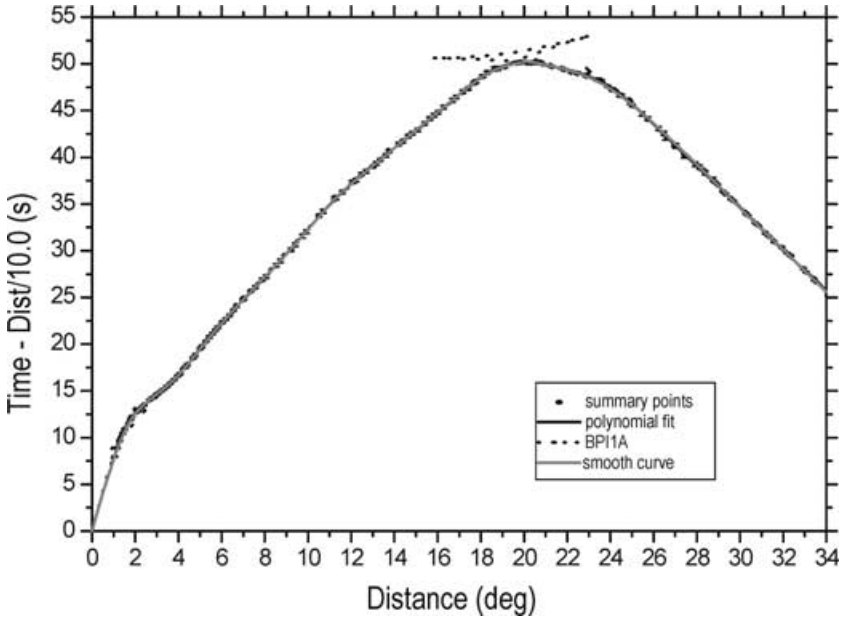

Figure 6. Plots of reduced traveltime data ($V_{red} = 10.0$ km s^{-1}) from the summary value technique (circles with error bars) overlain with smoothed curve from the spline algorithm of Reinsch (1967), polynomial fit (solid line) and model BPI1A (dotted line). Note that the agreement between the curve fits is so close that it is difficult to distinguish them.

ray tracing was used to refine the model by fitting curves of both the reduced traveltimes and slownesses generated from the summary values method to those from ray tracing (Figs 6 and 7).

DETERMINATION OF MODEL UNCERTAINTIES

In general, the wavespeed value at a particular depth cannot be uniquely determined. However, for a particular depth, one can consider determining the wavespeed within certain error bounds (e.g. Wiggins *et al.* 1973; Walck 1984). In this work, our determination of model uncertainties depends primarily on being able to choose a path of integration for slowness that is consistent with both the lower and upper confidence limits of the traveltime observations. The main objective for defining the bounds is to find paths that will give maximum and minimum wavespeeds for a particular depth that enclose a region within which the correct values have a 95 per cent chance of lying. Therefore we used both errors in summary points and cumulative errors in baseline corrections at a particular distance from our traveltime observations, to obtain 95 per cent confidence limits. Whereas the bounds given by Wiggins *et al.* (1973) define a region within which the solution may lie, they

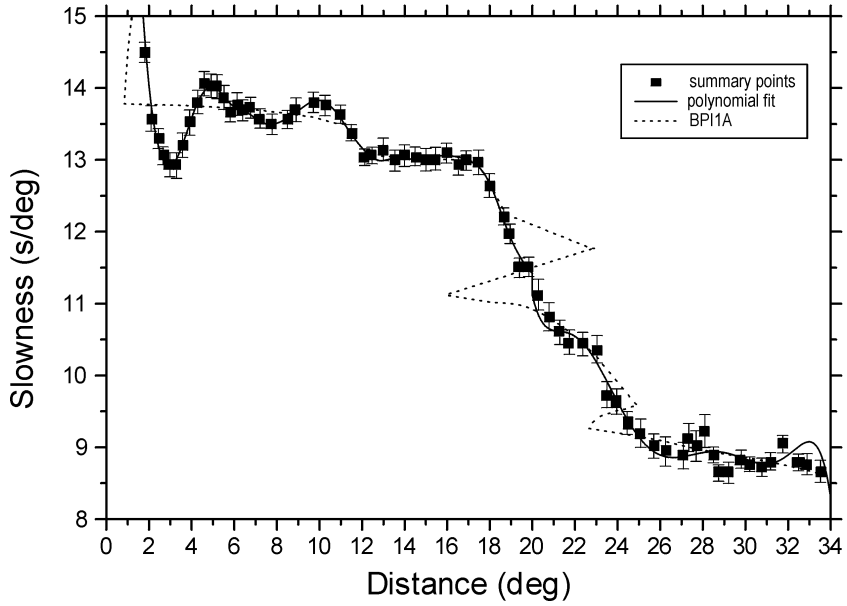

Figure 7. Plots of p-Δ data from the summary value technique (squares with error bars), two polynomials intersecting at 19.61° (solid line) and model BPI1A (dotted line).

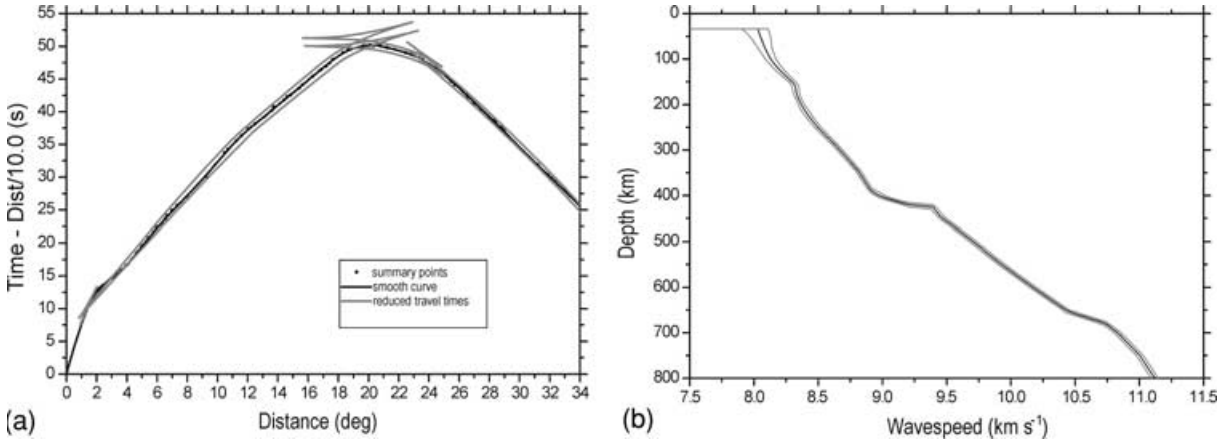

Figure 8. (a) Summary points and spline fit to the data (black line), bounded by reduced traveltime curves (thick dark grey lines) matching the lower and upper limits of the spline fit, $V_{red} = 10.0$ km s^{-1}, but perturbed to allow for the triplications for the 410 and 670 km discontinuities. (b) 95 per cent confidence limits for model BPI1A (dark grey lines) based on the assumption that the sharpness of the 410 and 670 km discontinuities is correct in each case. The error bounds were found under the assumption of fixed crustal wavespeeds to Moho depth (34 km) and have an average deviation of ±0.03 km s^{-1}.

are non-probabilistic in the sense that increasing the number of observations does not reduce the bounds. We have used a different approach that is statistical, resulting in a closing up of the confidence limits as the number of observations increases. These errors were added and subtracted from the spline fit to the data (black smooth curve in Fig. 8a), and an envelope was drawn around these paths. We then perturbed model BPI1A and used ray tracing to generate reduced traveltimes to match them with curves from the upper and lower limits of the spline fit as shown in Fig. 8(a). During perturbation of model BPI1A, we fixed crustal wavespeeds and Moho depth, and derived errors for the structure of the earth below the Moho down to 800 km depth. The resultant wavespeed envelope, corresponding with the two paths is shown in dark grey colour in Fig. 8(b), and the intervals just below the Moho depth, where the dark grey limits spread away from the model BPI1A (black line) indicate larger deviations (±0.12 km s^{-1}) compared to the rest of the model that shows an average deviation of ±0.03 km s^{-1}. The larger deviation below the Moho is influenced by the 'hump' observed in the data (Fig. 4) and by fixing crustal wavespeeds and Moho depth. The results given by the dark grey bounds (Fig. 8b) should be regarded as 95 per cent confidence limits on our knowledge of the weighted average wavespeed structure of the upper-mantle, transition zone and uppermost lower mantle of this region. We should expect these bounds to be improved considerably, as more data become available.

RESULTS AND DISCUSSION

To obtain detailed structure of the transition zone, we need to locate as accurately as possible the positions of the later branches and cusps of the triplications associated with the 410 and 670 km discontinuities. The observed records as shown by a composite record section of vertical-component *P* waveforms in Fig. 9(a) do not show convincingly the existence of the later branches when compared with

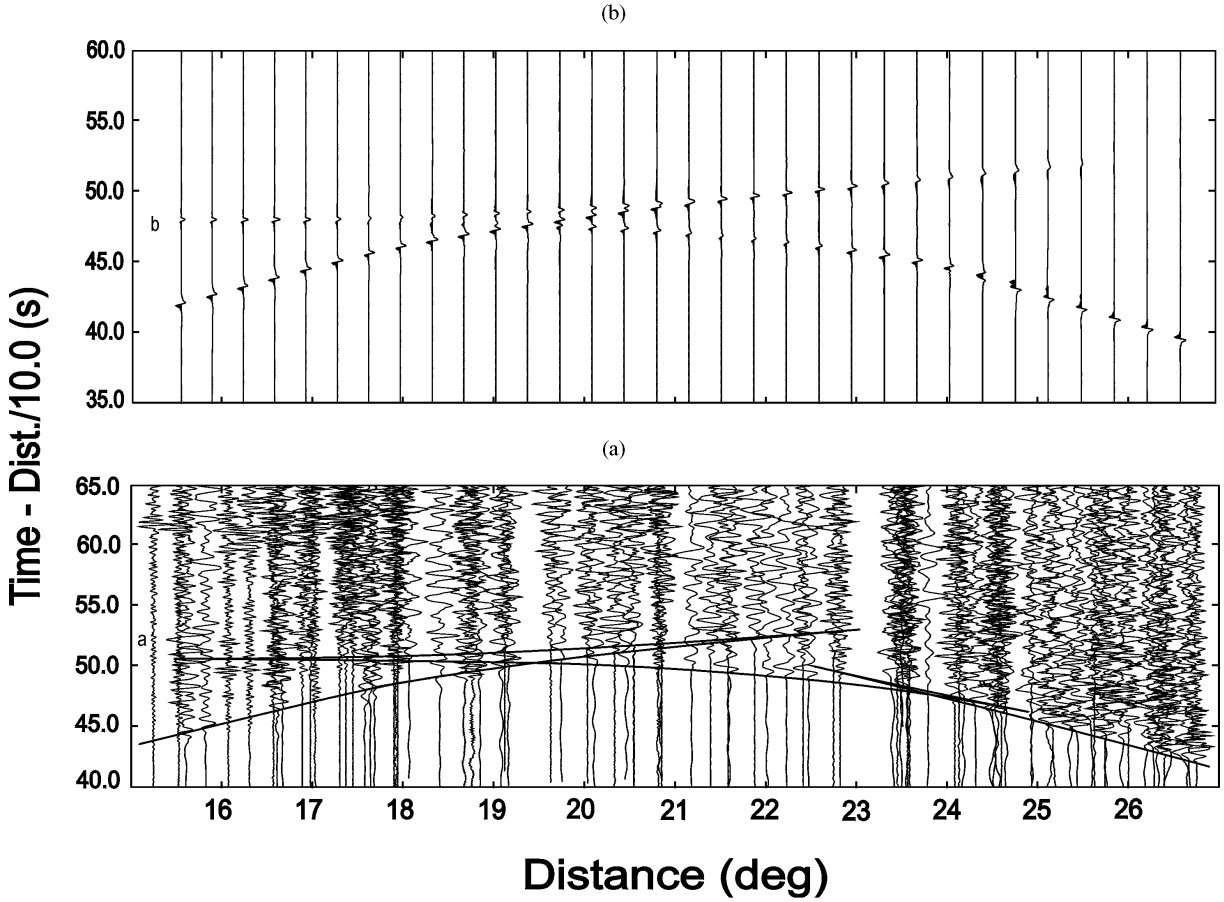

Figure 9. (a) Composite record section of vertical-component *P* waveforms from six different events (events 97264, 97283, 98064, 98087, 98116 and 98287 in Table 1), spanning distances greater than 15° but less than 27°. The waveforms have been band-pass filtered from 0.4–4.0 Hz and are overlain with the reduced travel-time curve from model BPI1A ($V_{red} = 10.0$ km s^{-1}). (b) Synthetic record section predicted by model BPI1A and filtered between 0.4–4.0 Hz.

the synthetic record section in Fig. 9(b), predicted by the final model BPI1A. This is because of the strong *P* coda following the *P* onset that makes the identification of later phases difficult.

If incoherent noise can be removed, it should be possible to identify later arrivals on the composite record section when the later arrival amplitudes are well separated in time as shown in Fig. 9(b). The PWS technique was used to achieve this. Some of the contributing factors to lack of clarity of later phases are weak signals, scattering, and multipathing effects due to complicated earth structure, complex source functions, regions of high attenuation and poor resolution of overlapping arrivals (Mereu 1975). Scattered waves in particular reach the earth's surface after the earliest *P* arrival and contribute to the build-up of the *P* coda, which, in turn, obscure the later phases of interest. All the first-arrival times used in the travel-time analysis from both the South African and Kaapvaal networks are shown in Fig. 3 and are overlain with the reduced traveltime curve from model BPI1A ($V_{red} = 10.0$ km s^{-1}). In addition, Figs 3 and 9(a) show upper mantle triplications for both the 410 and 670 km discontinuities, with crossover points between first arrival branches at distances of approximately 19.61° and 23.92°, respectively.

Figs 10(a) , (b) and (c) show results from stacking seismograms from different combinations of stations at different slownesses, for a particular earthquake to enhance coherent information and diminish incoherent noise. We compare results from a linear stack (L) and those from the PWS. In these figures, the PWS distinctly separates the first arrival from the later arrival branches in comparison with the linear stack results. Therefore, the PWS technique has resulted in an improved resolution to identify later *P* wave arrivals of different slownesses associated with upper-mantle triplications for both the 410 and 670 km discontinuities. On the plots of the PWS, markers T1 and T2 show the first and second arrival branches, respectively. The amplitudes of the PWS are smaller than or equal to the amplitudes of the linear stack since the coherence weight does not become larger than one (Schimmel & Paulssen 1997).

Fig. 10(a) shows stacked results of seismograms from fourteen stations that recorded an earthquake from Prince Edward Island region (event 97118 in Table 1), whereas Fig. 10(b) shows stacked results of seismograms from six stations that recorded an earthquake from South of Africa (event 97253a in Table 1). The distance ranges for the recording stations were 21.15–22.76° and 21.05–23.11°, for the Prince Edward Island and the South of Africa earthquakes, respectively. Furthermore, the pivot point distances for stacking (i.e. the distances of the stacks that give the correct relative traveltimes of the branches, which were chosen to be close to the middle of the distance range for the input seismograms) were 21.95° and 21.99°, for the Prince Edward Island and the South of Africa earthquakes, respectively. Both events gave best results for later arrivals at relative slownesses (p) of 0 and −1.20 s deg^{-1} (i.e. higher slownesses). The second branches arrived 2.26 and 2.01 s after the first arrival branches, for the Prince Edward Island and the South of Africa events, respectively. The first arrival branch (T1) has a depth of penetration within the transition zone, while the second

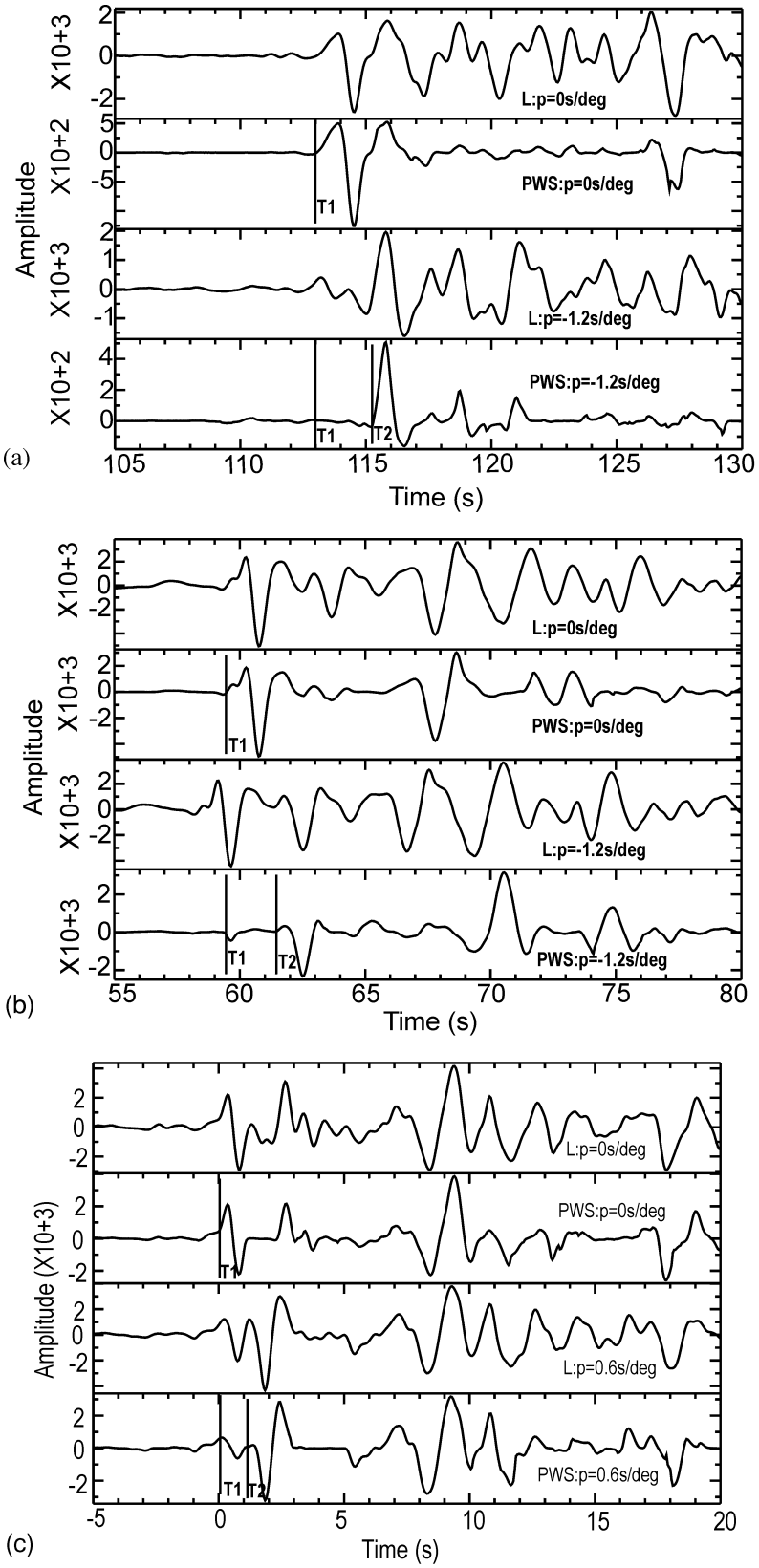

Figure 10. Stacked data from vertical-component *P* waveforms. The seismograms have been band-pass filtered from 0.4–4.0 Hz and are stacked at different relative slowness (p), with results from the linear stack (L) and phase-weighted stack (PWS). Markers T1 and T2 show the first and later arrival branches, respectively. (a) Stack of 14 seismograms of an earthquake from the Prince Edward Island region (event 97118 in Table 1) for epicentral distance ranges of 21.15° through 22.76° with the pivot point distance of 21.95°. (b) Stack of six seismograms of an earthquake from the region South of Africa (event 97253a in Table 1) for epicentral distance ranges of 21.05° through 23.11° with the pivot point distance of 21.99°. (c) Stack of five seismograms of the earthquake from Prince Edward Island region (event 97118 in Table 1) for epicentral distance ranges of 24.44° through 25.26° with the pivot point distance of 24.66°.

Table 2. Comparison of differences between low and high slowness arrival times measured using the phase-weighted stack from an earthquake that occurred west of Cape Town, with those measured from synthetic seismograms computed for model BPI1A using the WKBJ technique.

Station	Receiver distance (deg)	Measured time (s)	Synthetics time (s)
sa27	17.11	2.93	3.52
lbtb	17.36	2.88	3.30
sa33	17.49	2.63	3.00
sa28	17.70	2.94	2.78
sa45	17.85	2.92	2.70
sa40	18.00	2.90	2.41
sa46	18.57	2.66	1.85
sa42	19.70	−0.65	−0.59
sa51	19.91	−0.71	−0.93
sa155	20.65	−1.34	−1.11
sa57	21.81	−1.48	−1.40

branch (T2) has travelled above the transition zone. These branches are associated with the 410 km discontinuity. Another PWS result showing the branches associated with the 670 km discontinuity is shown in Fig. 10(c) from the Prince Edward Island event. The distance range for the recording stations was 24.44–25.26° and the seismograms shown were stacked at relative slownesses of 0 and 0.6 s deg^{-1}, at a pivot point distance of 24.66°. The second branch (T2) arrived approximately 1 s after the first arrival branch (T1). In this case, the first and second arrival branches have depths of penetration below and within the transition zone respectively. The PWS time picks (or later arrivals) are incorporated in the traveltimes, to associate them with traveltime branches. Representative results for synthetic seismograms were generated to compare with measured times from an earthquake that occurred west of Cape Town (event 98287 in Table 1) and are listed in Table 2. The correlation between the relative times from the observed (generated by varying the pivot distance in the stacks) and synthetic seismograms is good.

In Fig. 11, *P* wave traveltimes are plotted using a reduction wavespeed of 10.0 km s^{-1} to compare time picks from both the first and later arrival branches with those predicted by models BPI1A and SATZ (Zhao *et al.* 1999). The SATZ and BPI1A models are critical in inferring the earth's structure below southern Africa. The example of the *P* wave reduced traveltimes (Fig. 11) is from an earthquake that occurred in the Lake Tanganyika region (event 98087 in Table 1). Both the first and later arrival times corrected for origin time bias correlate less well with those from the BPI1A model than other events and form outliers in Fig. 3. At shorter distances the first arrivals are early relative to BPI1A times but later than those predicted by SATZ. The later arrival times reveal extensions of branches refracted above and below the 410 km discontinuity in Fig. 11.

It is interesting that the times from the Lake Tanganyika event are faster than those predicted by BPI1A at short distances where they are influenced predominantly by upper-mantle structure, are in good agreement when the first arrivals have emerged from the transition zone but tend to be later at larger distances where the *P* arrivals have emerged from the lower mantle. For this event, there is clearly a bias towards the times predicted by the SATZ model, which is what one would expect because the source receiver paths are closer to the region of the mantle studied by Zhao *et al.* (1999). In the future we hope to have enough data to derive separate models for events to the north and south of the network, because there are clearly regional differences in times that persist to transition zone depths (see Figs 2 and 3).

The final traveltime curve from model BPI1A computed by ray tracing is compared with the results from the summary value technique (Fig. 6). The fit is not quite perfect because the curve fit shows a region where the slowness increases slightly with increasing distance. This had to be smoothed out prior to inversion, and because the initial smooth model from the Herglotz–Wiechert inversion has been perturbed by introduced discontinuities to explain the results of PWS and to fit the synthetics. Furthermore, a good fit has been achieved in Fig. 7, as shown by the plots of slowness data from the summary values technique, polynomial fit and model BPI1A. At around 19.61° in Fig. 7, the polynomial fit (solid line) shows a kink

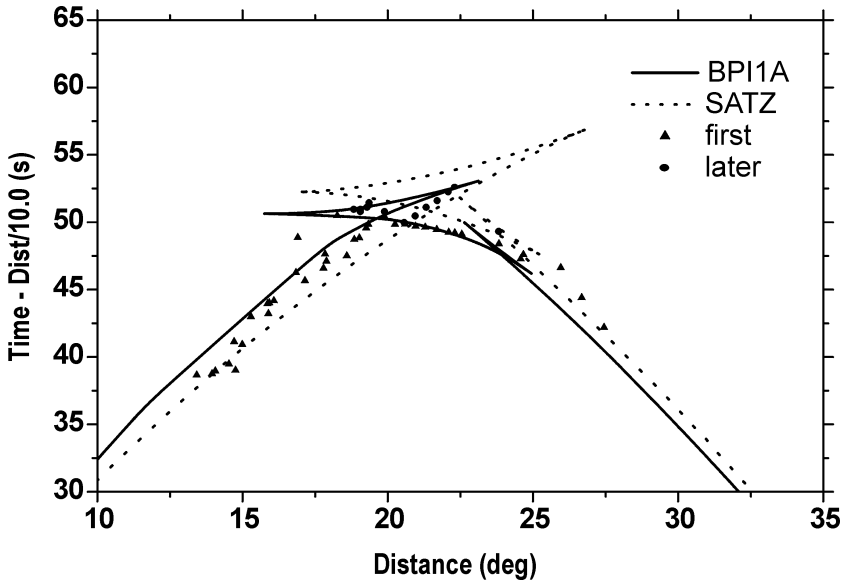

Figure 11. *P* wave reduced traveltimes ($V_{red} = 10.0$ km s^{-1}) from an earthquake that occurred in the Lake Tanganyika region (event 98087 in Table 1). The plot shows first arrival times (triangles) and later arrival times from PWS (circles) overlain by traveltimes calculated from models BPI1A (solid line) and SATZ (dotted line).

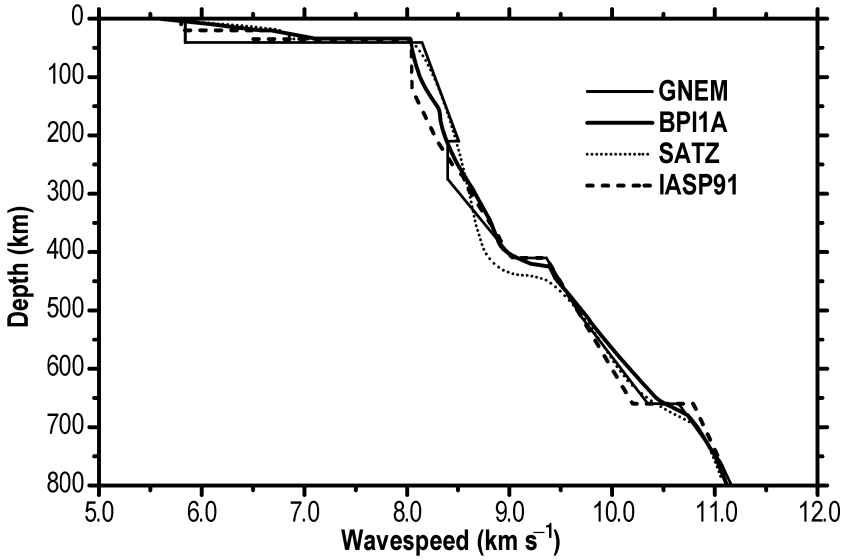

Figure 12. Comparison of *P* wavespeed models: IASP91 (Kennett 1991), SATZ (Zhao *et al.* 1999), GNEM (Ryberg *et al.* 1998) and BPI1A.

resulting from joining different polynomials, since a fourteenth-degree polynomial was fitted for distances less than 19.61° and a sixth-degree polynomial was fitted for times at distances greater than 19.61°.

A comparison is given in Fig. 12 of our derived model BPI1A (Table 3) with three other *P* wave models: the SATZ model published by Zhao *et al.* (1999), the IASP91 reference earth model (Kennett 1991) and the GNEM model (Ryberg *et al.* 1998). The model BPI1A has low positive wavespeed gradients below the Moho, faster seismic wavespeeds than those of the IASP91 model but slower than those of the SATZ model of Zhao *et al.* (1999) between the Moho and a depth of about 270 km, at which the three models converge. GNEM has lower wavespeeds than the other three models between depths of 270 km and the 410 km discontinuity. In comparison with the GNEM model, the BPI1A model lacks a well-pronounced low-wavespeed zone above depths of approximately 375 km (Fig. 12). This might be a regional feature, which characterizes the mantle above the transition zone in northern Eurasia, but is absent in southern Africa.

In Fig. 12, models BPI1A and IASP91 are very similar from depths of about 270 km to the 410 km discontinuity, although this discontinuity is about 10 km deeper than in IASP91. They have faster seismic wavespeeds at these depths compared with those of the SATZ model, which are systematically slower at the same depths. It is not clear why the SATZ model should have significantly slower wavespeeds at these depths (Fig. 12). However, models BPI1A and SATZ reveal a transitional 410 km discontinuity whereas IASP91 has an abrupt 410 km discontinuity. Within the transition zone, the two southern African models, BPI1A and SATZ, have similar mantle wavespeeds, whereas the IASP91 model has slower wavespeeds below depths of about 500 km. Resolution of the present data set is not sufficient to confirm or rule out the existence of the 520 km discontinuity. However, models IASP91 and GNEM have a sharp 670 km discontinuity while models BPI1A and SATZ show a transitional 670 km discontinuity (Fig. 12). The narrow and weakly-defined triplication associated with the 670 km discontinuity allows us to infer that this discontinuity is on average transitional. Although GNEM has a sharp 670 km discontinuity, Ryberg *et al.* (1998) suggested that models with a smaller wavespeed step (∼50 per cent) across the 670 km discontinuity or with a transitional 670 km discontinuity of several tens of kilometres thickness provide the best fit to their observed data for the triplication associated with this discontinuity in the Eurasia region.

The wavespeed gradients from model BPI1A reveal that the transition zone is approximately 248 km in thickness, while results from Zhao *et al.* (1999) show a slightly thinner transition zone, approximately 230 km. We observe a close agreement when comparing our estimate of the transition zone thickness beneath southern Africa with the global average thickness of 241 km from Flanagan & Shearer (1998). This suggests that there is little thinning of the transition zone and hence that temperatures are not likely to be elevated between depths of 400 and 700 km in this region (e.g. Nyblade *et al.* 2000). However, the wavespeeds in model BPI1A are a little higher on average than in the other models suggesting, for example, depletion in iron relative to other regions. This would result in lower densities within the transition zone, which might cause part of the buoyant uplift of the overlying upper-mantle and crust to provide the high elevation of the Kaapvaal craton. Below the transition zone to depths slightly above 750 km, both the BPI1A and SATZ models have similar mantle wavespeeds, but the IASP91 model has significantly higher wavespeeds. All four models have similar wavespeeds below 750 km depth (Fig. 12). The traveltimes from events 97253a, 97253b, 98064 and 98116 in Table 1, reveal that the mantle below the transition zone, with turning points shown as open circles in Fig. 2, below both the continental and oceanic lithospheres, has similar properties. In comparing the *P* wavespeeds derived in this study with those of the GNEM model, the mantle within the transition zone and lower mantle to depths of 800 km beneath southern Africa and that beneath northern Eurasia exhibit similar wavespeed variations.

The 670 km discontinuity is consistent with a phase transformation from γ-spinel to perovskite and magnesiowüstite, provided the mantle has a predominantly olivine composition (e.g. Ryberg *et al.* 1998). Because the 410 km discontinuity in model BPI1A closely matches that of the global average, then this discontinuity can probably be explained by the discontinuous reaction of olivine $+\gamma$-spinel to form the ß-phase (e.g. Jeanloz & Thompson 1983) but with possible small changes in major element abundance in

Table 3. Model BPI1A.

Depth (km)	Vp (km s^{-1})	Depth (km)	Vp (km s^{-1})	Depth (km)	Vp (km s^{-1})	Depth (km)	Vp (km s^{-1})
0	5.5800	190	8.3515	395	8.9422	600	10.1715
5	5.8500	195	8.3601	400	8.9759	605	10.1967
10	6.1200	200	8.3695	405	9.0222	610	10.2220
15	6.3270	205	8.3797	410	9.0777	615	10.2475
20	6.5665	210	8.3905	415	9.1409	620	10.2730
20	6.6704	215	8.4019	420	9.2071	625	10.2987
25	6.8238	220	8.4140	425	9.3918	630	10.3245
30	6.9772	225	8.4266	430	9.4057	635	10.3503
34	7.1000	230	8.4398	435	9.4197	640	10.3762
34	8.0300	235	8.4536	440	9.4336	645	10.4022
40	8.0377	240	8.4678	445	9.4475	650	10.4280
45	8.0442	245	8.4826	450	9.4699	655	10.4655
50	8.0497	250	8.4979	455	9.4937	660	10.5163
55	8.0562	255	8.5137	460	9.5179	665	10.5747
60	8.0631	260	8.5311	465	9.5421	670	10.6299
65	8.0701	265	8.5485	470	9.5663	675	10.6851
70	8.0774	270	8.5659	475	9.5902	680	10.7373
75	8.0848	275	8.5833	480	9.6139	685	10.7610
80	8.0924	280	8.6007	485	9.6373	690	10.7847
85	8.1015	285	8.6181	490	9.6605	695	10.8068
90	8.1128	290	8.6370	495	9.6835	700	10.8307
95	8.1198	295	8.6527	500	9.7063	705	10.8480
100	8.1307	300	8.6684	505	9.7289	710	10.8653
105	8.1431	305	8.6840	510	9.7515	715	10.8826
110	8.1569	310	8.6997	515	9.7742	720	10.8999
115	8.1718	315	8.7154	520	9.7919	725	10.9172
120	8.1876	320	8.7311	525	9.8141	730	10.9345
125	8.2043	325	8.7468	530	9.8366	735	10.9518
130	8.2218	330	8.7624	535	9.8592	740	10.9690
135	8.2400	335	8.7781	540	9.8821	745	10.9864
140	8.2588	340	8.7938	545	9.9052	750	11.0037
145	8.2781	345	8.8104	550	9.9284	755	11.0153
150	8.2976	350	8.8216	555	9.9519	760	11.0269
155	8.3129	355	8.8328	560	9.9756	765	11.0384
160	8.3208	360	8.8440	565	9.9994	770	11.0500
165	8.3248	365	8.8552	570	10.0235	775	11.0615
170	8.3275	370	8.8664	575	10.0478	780	11.0731
175	8.3313	375	8.8776	580	10.0722	785	11.0846
180	8.3369	380	8.8888	585	10.0968	790	11.0961
185	8.3437	385	8.9009	590	10.1215	795	11.1077
		390	8.9175	595	10.1465	800	11.1192

comparison with some other regions. However, Fujisawa (1998) proposed a chemical boundary instead of a phase change from experimental results as the origin of this discontinuity, since the observed change in wavespeed is smaller than that predicted for a phase change in a mantle of uniform peridotitic composition.

CONCLUSIONS

The '410 km discontinuity' in model BPI1A occurs at ∼420 km depth, whereas the '670 km discontinuity' occurs at ∼668 km. High-gradient zones characterize the structure around the 410 and 670 km discontinuities. The estimated depths of the discontinuities are similar to those of the IASP91 and GNEM models, but the SATZ model has a much deeper 410 km discontinuity than any of the other three. The deeper 410 km discontinuity in SATZ may be caused by errors in event origin times rather than real differences in earth structure compared with other cratonic regions. Seismic wavespeeds of BPI1A within the transition zone are similar to or slightly higher than those in the SATZ and GNEM models which might indicate localised iron depletion, and hence lower average densities. The model BPI1A shows a prominent 410 km discontinuity, and a weakly defined 670 km discontinuity that is in agreement with the earlier results of Zhao *et al.* (1999) for a region of southern Africa farther north of the Kaapvaal craton.

The similarity in models BPI1A and SATZ below depths of 670 km, reveal that the uppermost lower mantle below both the continental and oceanic lithospheres has similar properties. The similarity in models BPI1A and GNEM between the depths of 375 and 800 km apart from slightly higher average wavespeeds for BPI1A for the transition zone reveal that the mantle beneath southern Africa and that beneath northern Eurasia exhibit similar properties at these depths. There are no indications of anomalous low wavespeed structure in our model within the mantle to depths of about 800 km that could be associated with an uplift of the African superswell due to higher temperatures. Hence, the source of this uplift would most likely reside below depths of 800 km (Gurnis *et al.* 2000), although the possible contribution of lower average densities in the transition

zone merits further consideration. Further work is in progress to develop the shear-wave equivalent of model BPI1A.

ACKNOWLEDGMENTS

This research was supported by funding from the National Research Foundation (South Africa), the National Science Foundation (USA), the University Research Council of the University of the Witwatersrand, and by mining companies operating in southern Africa. The University of Botswana sponsored RES. MTOK received financial support from the Government of Botswana and from the Kellogg Foundation (USA). Event 97180 of Table 1 was located by James King (University of Botswana) and Teresia Nguuri (University of the Witwatersrand). We are very grateful to Martin Schimmel, and to Andrew Gowman and John Amor who provided the PWS and synthetic seismogram software, respectively. We are grateful to those who made the Kaapvaal project successful. We would like to thank Hanneke Paulssen for her helpful comments during the review of this manuscript and also the anonymous reviewer.

REFERENCES

Aki, K. & Richards, P.G., 1980. Quantitative Seismology: Theory and methods, Vol. 2, Freeman, W.H., San Francisco.

Bolt, B.A., 1978. Summary value smoothing of physical time series with unequal intervals, *Journal of Computational Physics,* **29,** 357–369.

Carlson, R.W., Grove, T.L., de Wit, M.J. & Gurney, J.J., 1996. Program to study crust and mantle of the Archaean craton in southern Africa, *EOS, Trans. Am. geophys. Un.,* **77,** 273–277.

Cattermole, P.A., 1994. Upper mantle discontinuities beneath southern Africa—Results of the analysis of *P* to *S* converted phases, *MSc Thesis*, University of the Witwatersrand, Johannesburg.

Chapman, C.H., 1978. A new method for computing synthetic seismograms, *Geophys. J. R. astr. Soc.,* **54,** 481–518.

De Wit, M.J. *et al.*, 1992. Formation of an Archaean continent, *Nature,* **357,** 553–562.

Dey, S.C., Kennett, B.L.N., Bowman, J.R. & Goody, A., 1993. Variations in upper mantle structure under northern Australia, *Geophys. J. Int.,* **114,** 304–310.

Flanagan, M.P. & Shearer, P.M., 1998. Global mapping of topography on transition zone velocity discontinuities by stacking SS precursors, *J. geophys. Res.,* **103,** 2673–2692.

Fujisawa, H., 1998. Elastic wave velocities of forsterite and its spinel form and chemical boundary hypothesis for the 410 km discontinuity, *J. geophys. Res.,* **103,** 9591–9608.

Green, R.W.E., Webb, S.J. & Wright, C., 1995. Broadband seismic studies in southern Africa, *South African Journal of Science,* **91,** 234–239.

Gurnis, M., Mitrovica, J.X., Ritsema, J. & van Heijst, H.J., 2000. Constraining mantle density structure using geological evidence of surface uplift rates: The case of the African superplume, *Geochem. Geophys. Geosyst.,* Vol. 1, paper number 1999GC000035.

Jeanloz, R. & Thompson, A.B., 1983. Phase transitions and mantle discontinuities, *Rev. Geophys.,* **21,** 51–74.

Jeffreys, H., 1937. On the smoothing of observed data, *Proc. Cambridge Philos. Soc.,* **33,** 444–450.

Jeffreys, H., 1961. Theory of Probability, Oxford University Press, Oxford.

Kennett, B.L.N. (Ed.), 1991. IASPEI 1991 Seismological Tables, Research School of Earth Sciences, Australian National University, Canberra, Australia.

Kennett, B.L.N., Gudmundsson, O. & Tong, C., 1994. The upper mantle *S* and *P* velocity structure beneath northern Australia from broadband observations, *Phys. Earth planet. Int.,* **86,** 85–98.

McQuillin, R., Bacon, M. & Barclay, W., 1984. An Introduction to Seismic Interpretation: Reflection Seismics in Petroleum Exploration, Graham and Trotman Limited, London.

Mereu, R.F., 1975. A study of the effect of Q on the observation of upper mantle travel-time branches using adaptive processing techniques, in *Exploitation of Seismograph Networks,* pp. 471–488, ed. Beauchamp, K.G., Proceedings of NATO Advanced Study held at Sandefjord, Norway, April 22–May 3, 1974, Noordhoff, Leiden, The Netherlands.

Nyblade, A.A., Birt, C., Langston, C.A., Owens, T.J. & Last, R.J., 1996. Seismic experiment reveals rifting of craton in Tanzania, *EOS, Trans. Am. geophys. Un.,* **77,** 517–521.

Nyblade, A.A., Knox, R.P. & Gurrola, H., 2000. Mantle transition zone thickness beneath Afar: implications for the origin of the Afar hotspot, *Geophys. J. Int.,* **142,** 165–169.

Reinsch, C.H., 1967. Smoothing by spline functions, *Numer. Math.,* **10,** 177–183.

Ryberg, T., Wenzel, F., Egorkin, A.V. & Solodilov, L., 1998. Properties of the mantle transition zone in northern Eurasia, *J. geophys. Res.,* **103,** 811–822.

Schimmel, M. & Paulssen, H., 1997. Noise reduction and detection of weak, coherent signals through phase-weighted stacks, *Geophys. J. Int.,* **130,** 497–505.

Vinnik, L.P., Green, R.W.E. & Nicolaysen, L.O., 1996. Seismic constraints on dynamics of the mantle of the Kaapvaal craton, *Phys. Earth planet. Int.,* **95,** 139–151.

Walck, M.C., 1984. The *P*-wave upper mantle structure beneath an active spreading centre: the Gulf of California, *Geophys. J. R. astr. Soc.,* **76,** 697–723.

Wiggins, R.A., McMechan, G.A. & Toksöz, M.N., 1973. Range of earth structure nonuniqueness implied by body wave observations, *Rev. Geophys. and Space Physics,* **11,** 87–113.

Wright, C., 1999. The LSDARC method of shallow seismic refractor investigation, and the resolution of lateral variations in wavespeed, in 6th Biennial Conference and Exhibition of the South African Geophysical Association, Cape Town, South Africa, 28 September–1 October, 1999, paper 4.1, p. 12.

Wright, C., Webb, S.J. & Nguuri, T.K., 1997. Broadband seismological studies on the Kaapvaal craton: Data acquisition and research objectives (extended abstract), South African Geophysical Association, Fifth technical meeting 29th–30th September 1997, Swakopmund, Namibia, 189–192.

Wright, C., Kwadiba, M.T.O., Kgaswane, E.M. & Simon, R.E., 2002. The structure of the crust and upper mantle to depths of 320 km beneath the Kaapvaal craton, from *P* wave arrivals generated by regional earthquakes and mining-induced tremors, *Journal of African Earth Sciences* (in press).

Zhao, M., Langston, C.A. & Nyblade, A.A., 1999. Upper mantle velocity structure beneath southern Africa from modeling regional seismic data, *J. geophys. Res.,* **104,** 4783–4794.